

Finite Volume Simulations of the Collision of Viscoelastic Droplets using Adaptive Re-meshing and Explicit Interface Tracking

Kyle G. Mooney, David P. Schmidt*

Dept. of Mechanical and Industrial Engineering, University of Massachusetts Amherst, USA
schmidt@acad.umass.edu

Abstract

The effectiveness of gelled fuel jet impingement, food production, and polymer-based spray coatings can depend on the atomization and droplet collision behavior of fluids with complex rheology. Non-Newtonian effects such as shear-thinning, shear thickening, and viscoelastic extensional hardening (usually a consequence of macro-molecular interactions) could alter collision outcomes as well as drop-to-drop mixing rates. Extensional hardening specifically has been shown to promote the stability of liquid ligaments, a structure often formed during the transients of a droplet collision. In this study, direct numerical simulations of single phase viscoelastic droplet collisions are performed within a finite volume framework. The free surface is modeled with an explicit moving mesh interface tracking method, allowing highly accurate calculation of surface curvature, which is increasingly important with decreasing Weber number. In this method, the boundary of the computational domain acts as the free surface with pressure and velocity field boundary conditions applied directly. Control volume distortion due to large boundary deformation is minimized using quality-driven node smoothing and a localized edge reconnection algorithm specific to tetrahedral meshes. Mesh-to-mesh vector and scalar field mapping error is reduced using a recently developed second-order accurate conservative interpolation scheme. The free surface and viscoelastic implementations are validated against analytical solutions and experimental data. Simulation results capture rapid growth in viscoelastic stress during ligament drainage in areas surrounding pinch-off points. In addition fluid ligaments have shown to be increasingly stable with higher Deborah numbers.

Introduction

Computational models of dense sprays must consider droplet collision and coalescence to accurately capture drop size distribution [1], [2]. Experimental and modeling-based studies of binary droplet collisions over the past decades have shed considerable light onto the topic and, in general, improved the understanding of a spray's behavior after primary atomization. Canonical experiments involving Newtonian droplet collisions have been performed by Qian and Law [3], Ashgriz and Poo [4], and Willis and Orme [5] to name a few. Research concerning the more specific field of non-Newtonian droplet dynamics is primarily motivated by the development of precision printing and coating technology [6], and more recently, interest in the injection characteristics of gelled fuels [7].

Computational work on shear-thinning droplet collisions [8] [9] argue that in low Weber number collision regimes, non-Newtonian rheological modeling can be replaced by a single equivalent effective viscosity. This type of model order reduction may not be possible for viscoelastic droplets, as extensional hardening effects are a function of the deformation history of the fluid. Due to these strain history effects, a differential evolution equation for the viscoelastic stress (arranged in the form of a symmetric second order tensor) is solved in addition to the Navier-Stokes equation. The number of experimental and computational studies of specifically viscoelastic droplet collision systems (drop-drop as well as drop-wall interaction) is limited [10] [11]. In general viscoelastic fluids tend to exhibit large Trouton ratios which is the ratio of effective extensional to shear viscosities, a consequence of long chain macro-molecular alignment.

The relevant kinematic parameters of a collision of two equal sized droplets are illustrated in Fig.1. Here, U is the relative velocity, and D is the diameter. The impact parameter $\chi = b/D$ represents how head-on ($\chi = 0$) or obliquely ($\chi = 1$) a collision occurs. Collision outcomes (coalescence or separation type modes) can be predicted for Newtonian fluids based on these parameters. Due to the introduction of viscoelastic effects, a Deborah number can be defined as $De = \lambda U/D$, which represents the ratio of the stress relaxation time (λ) to the characteristic time scale of the flow. The collision Reynolds and Weber number are defined as $(\rho DU/\mu)$ and $(\rho DU^2/\sigma)$ respectively where ρ is the density and σ is the surface tension.

All CFD modeling in this work uses OpenFOAM, the open-source and community driven computational continuum mechanics library described in Weller et al. [12]. Flow field solutions are computed on an unstructured tetrahedral mesh using a collocated finite volume discretization approach.

*Corresponding author: schmidt@acad.umass.edu

Numerical Methods

Low Weber number flows are dominated by interfacial surface tension forces. In order to accurately and efficiently capture these surface based forces, this work employs a less common interface treatment entitled moving mesh interface tracking (MMIT). Here, the tessellated boundary of the domain acts as the free surface and moves in a Lagrangian fashion as the surface deforms through time. The specific free surface implementation is described in great detail by Tukovic and Jasak [13]. This Lagrangian style free surface treatment readily distorts the interior and surface mesh, harming numerical stability. In order to maintain a high quality mesh and allow extensive topological deformation, cell distortion is re-actively corrected with two approaches: node smoothing and edge reconnection.

Mesh smoothing is a process by which nodes are manually displaced in a manner that improves the overall quality of the surrounding cells. In instances of more extreme boundary deformation, where node smoothing alone cannot maintain adequate cell quality, mesh connectivity itself is altered. The connectivity operations used to improve mesh quality also control local and global mesh resolution. Further details on the tetrahedral adaptive mesh methods used can be found in work by Dai and Schmidt [14]. Vector and scalar fields are locally re-mapped following topological changes and are done so with second order accuracy using methods recently developed by Menon and Schmidt [15]. Tensor fields are limited to first order accurate local re-mapping. These adaptive mesh routines are implemented in a general sense such that they are applicable to both internal and external deforming boundary flow problems in addition to the free surface simulations presented in this work.

The mesh smoother displaces nodes and thus mesh faces as it optimizes the global mesh quality. These motions are taken into account by calculating the volume of the polygons swept by internal faces before and after the smoothing operation. Face fluxes are then corrected be relative to the mesh motion. Due to errors in this swept volume calculation, the space conservation law, shown in equation Eq.1, is not satisfied exactly. That is, the change in volume (V) of a cell does not exactly equal the sum of the calculated swept volumes of the faces. Here, \mathbf{n} is the unit face normal and \mathbf{v}_s is the face velocity.

$$\frac{d}{dt} \int_V dV - \int_S \mathbf{n} \cdot \mathbf{v}_s dS = 0 \quad (1)$$

It has been observed that this residual error manifests as numerical diffusion proportional to the total swept volume. Efforts are currently underway to calculate these polygonal swept volumes exactly and satisfying space conservation. More background on swept volume computation and its role in free surface flows can be found in the work by Apsley and Hu[16].

Accuracy of the free surface treatment is validated via the simulation of a 3D spherical mode-2 oscillating droplet. Analytical solutions for the viscous decay time constant and theoretical period are derived from perturbation analysis by Lamb [17]. The drop was given an initial perturbation such that the ratio of the major and minor axes lengths of the oblate spheroid correspond to a 2% perturbation. Validation testing results are illustrated in Fig.2 and are in excellent agreement with the analytical decay and period solutions.

Macro-molecular interactions are modeled using the Phan-Thien-Tanner (PTT) constitutive stress formulation, named after the original developers [19]. This model takes the differential tensor based form:

$$f(\text{tr}(\boldsymbol{\tau}))\boldsymbol{\tau} + \lambda \overset{\nabla}{\boldsymbol{\tau}} = 2\eta\mathbf{D} \quad (2)$$

The symbol $\overset{\nabla}{(\cdot)}$ represents the upper-convected derivative, λ is the stress relaxation time of the fluid, and $\boldsymbol{\tau}$ is the viscoelastic stress tensor. The stress tensor $\boldsymbol{\tau}$ is symmetric with six unique components. $\overset{\nabla}{\boldsymbol{\tau}}$ is then defined as

$$\overset{\nabla}{\boldsymbol{\tau}} = \frac{D\boldsymbol{\tau}}{Dt} - \boldsymbol{\tau} \cdot \mathbf{L} - \mathbf{L}^T \cdot \boldsymbol{\tau} \quad (3)$$

\mathbf{L} represents the effective velocity gradient

$$\mathbf{L} = \nabla\mathbf{u} - \zeta\mathbf{D} \quad (4)$$

where $\nabla\mathbf{u}$ is the velocity gradient and ζ is a shear modifier which represents relative slip of polymer chains. The tensor \mathbf{D} is the symmetric rate of deformation tensor.

$$\mathbf{D} = \frac{1}{2}(\nabla\mathbf{u} + (\nabla\mathbf{u})^T) \quad (5)$$

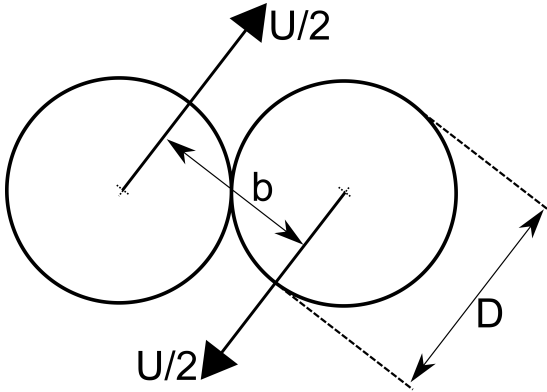
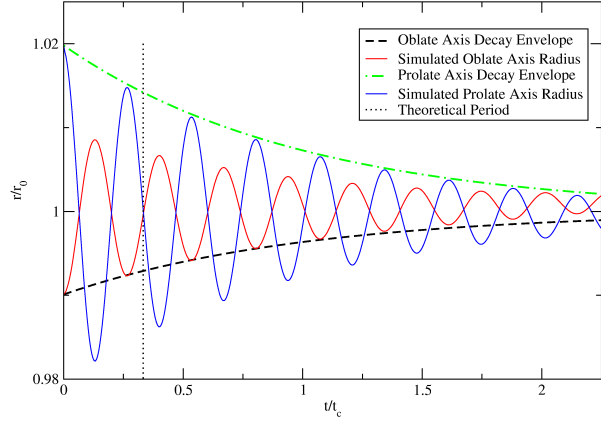


Figure 1: Droplet collision kinematics

Figure 2: Viscous decay envelope and analytical oscillation period of a simulation droplet. Axis lengths are normalized by the equivalent spherical radius r_0 , and time is normalized by the analytical time constant t_c .

The stress coefficient is

$$f(tr(\boldsymbol{\tau})) = 1 + \frac{\lambda\epsilon}{\mu_p} tr(\boldsymbol{\tau}) \quad (6)$$

where ϵ is an effective extensional viscosity modifier and used along with ζ as a fitting parameter. The effective polymer viscosity is μ_p and $tr()$ is the tensor trace operator. Because $f(tr(\boldsymbol{\tau}))$ is linear with respect to $\boldsymbol{\tau}$, this particular formulation is known as the linear Phan Thien Tanner (LPPT) model. This model was chosen specifically because it captures shear thinning and extensional thickening behavior. This implementation is part of a C++ rheological library developed for OpenFOAM by Favero et al [18].

Validation of the implemented PTT viscoelastic constitutive stress model is performed by recreating the experimental comparison performed by Favero et al. [18] and Azaiez et al. [20]. Viscoelastic stress and velocity profiles are sampled across a 4:1 planar contraction flow, described in detail by Quinzani et al. [21]. The working fluid consists of a low density polymer solution fit with single mode PTT parameters which is characterized along with relevant material properties in Favero et. al [18]. All lengths shown in the validation comparisons are normalized by the contraction height, h , where $h = 0.0032$ [m]. The case geometry is illustrated in Fig.3 with imposed symmetry boundary conditions about the centerline and no slip walls. Comparisons between experimental stress and velocity results and simulation solutions are illustrated in Fig.3-Fig.6. Values along the sample scan lines are computed via least squares interpolation from cell centered values. Viscoelastic stresses are captured to an acceptable accuracy and is comparable to the results of both the Favero and Azaiez investigations.

To help delay the destabilizing High Weissenberg number problem (HWNP) inherent in viscoelastic simulations, the momentum equation is augmented by the both-sides-diffusion method [22]. The final form of the incompressible momentum transport equation is shown in Eq.7 where ρ is the density, μ_s is the solvent viscosity, ϕ is the face flux, and p is the pressure. Here, all left-hand-side terms are treated implicitly while all right-hand-side momentum terms are treated explicitly.

$$\begin{aligned} \rho \left(\frac{\partial \mathbf{u}}{\partial t} + \nabla \cdot \phi \mathbf{u} \right) - (\mu_s + \mu_p) \nabla^2 \mathbf{u} \\ = -\nabla p + \nabla \cdot \boldsymbol{\tau} - \mu_p \nabla^2 \mathbf{u} \end{aligned} \quad (7)$$

The initial mesh configuration used for analysis in this work is illustrated in Fig.7 which consists of approximately 112,000 tetrahedra and a cylindrical drop-to-drop liquid connecting bridge whose length is $0.06 \cdot D$ and diameter is $0.25 \cdot D$. The bridge has the same material properties as the bulk liquid and serves to unify the computational domain before simulation start. Due to current software limitations, only a single contiguous domain

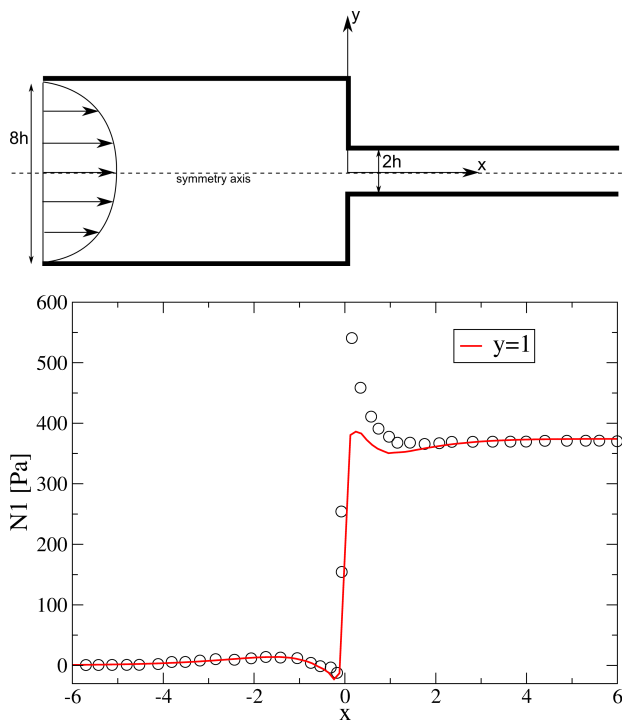


Figure 3: Top: Viscoelastic validation geometry setup for a 4:1 planar contraction. Note the coordinate origin location below the corner, aligned with the centerline. $Re = 0.56, De = 2.9$ [20, 18]. Bottom: Profile of the first normal stress difference $N_1 = \tau_{xx} - \tau_{yy}$ along $y = h$. Lines: simulation, Symbols: experiment [21].

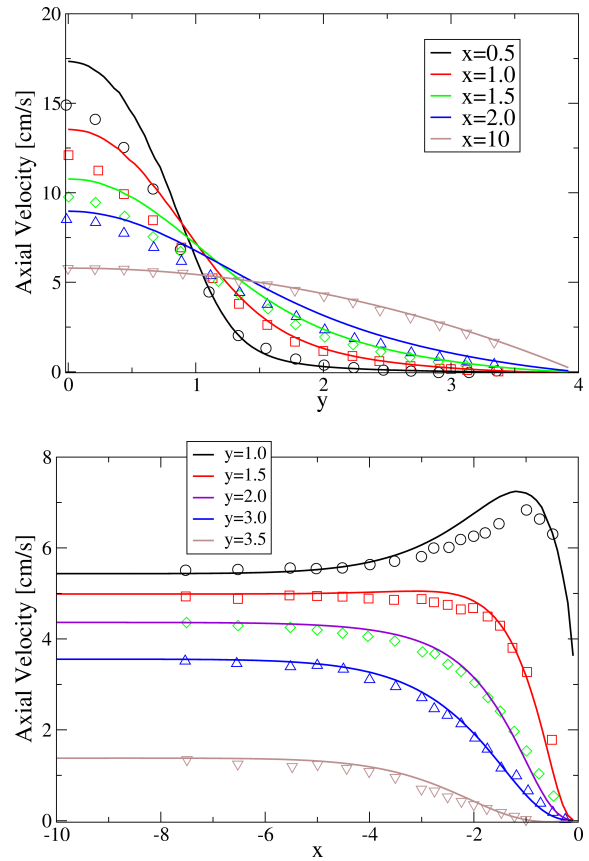


Figure 4: Profiles of the axis normal velocity in the upstream section. Lines: simulation, Symbols: experiment [21].

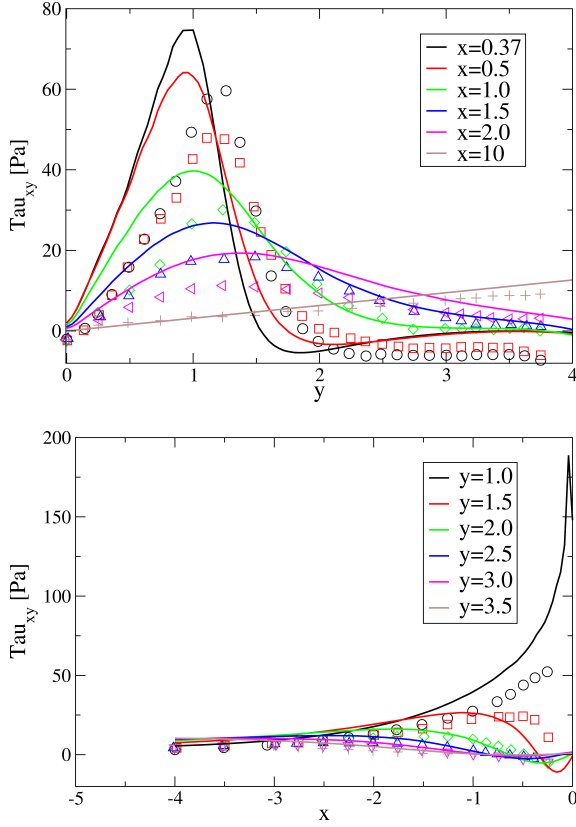


Figure 5: Profiles of the shear stress τ_{xy} in the upstream section. Lines: simulation, Symbols: experiment [21].

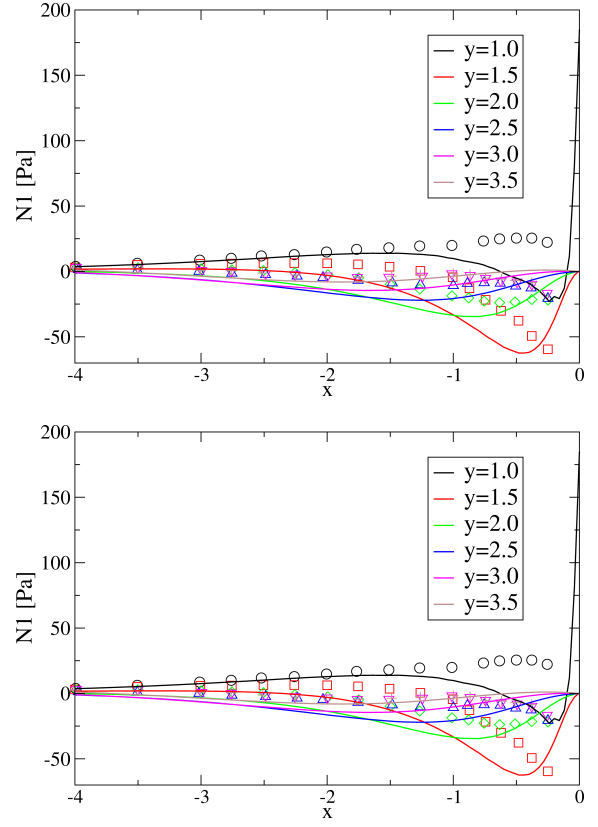


Figure 6: Profiles of the first normal stress difference $N_1 = \tau_{xx} - \tau_{yy}$ in the upstream section. Lines: simulation, Symbols: experiment [21].

is currently supported. The total number of cells in the domain change throughout the simulation and generally scales over time with the surface to volume ratio of the domain. Mesh independence is verified through the comparison of two identical collision configurations on a low and high density mesh (approx. $110k$ vs $440k$). A plot of the domain bounding box dimensions throughout a collision are plotted in Fig.8 and argue that the $110k$ cell mesh is adequately converged. The collision parameters used in this mesh study are identical to those of the case discussed in the following section. In order to isolate the effects of viscoelasticity on collisions, Re and We are held constant while De is varied by adjusting the stress relaxation time, λ . Note that Re is defined using μ_s , the solvent viscosity.

Results and Discussion

Time lapse images of a simulated viscoelastic droplet collision are displayed in Fig.9 along with relevant kinematic and flow parameters. This type of collision outcome is considered a *stretching separation* mode. For collisions at this De , viscoelastic effects do not come into play until the final stages of the collision. It is in these final moments that surface driven instabilities initiate the ligament drainage process and begin to collapse the surface onto a point. This cylindrical drainage takes the form of a rapid extensional flow which quickly increases the Trouton ratio effects of the extra viscoelastic stress model. Sample scans of the first normal stress difference ($N_1 = \tau_{xx} - \tau_{yy}$) along a line co-axial with the ligament orientation of frames A-D from the time lapse images are shown in Fig.10. There is a rapid jump in viscoelastic stress as the two ligament pinch points drain and extensional gradients increase.

Deborah number effects on the late stages of a droplet collision can be observed in Fig.11. Here, both the pinch points and the middle ligament are stabilized by additional viscoelastic stress; increasingly so in the higher De droplet. The higher De droplet's stability is evident by the thicker pinch points and a more cylindrical central ligament. Both frames are time-paired.

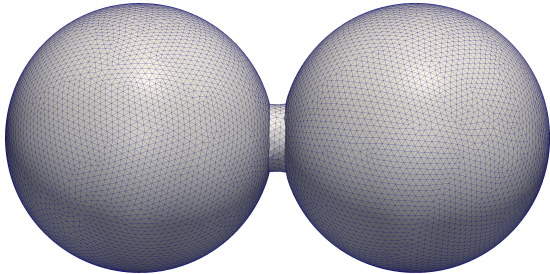


Figure 7: Illustration of the initial mesh used for all collision simulations.

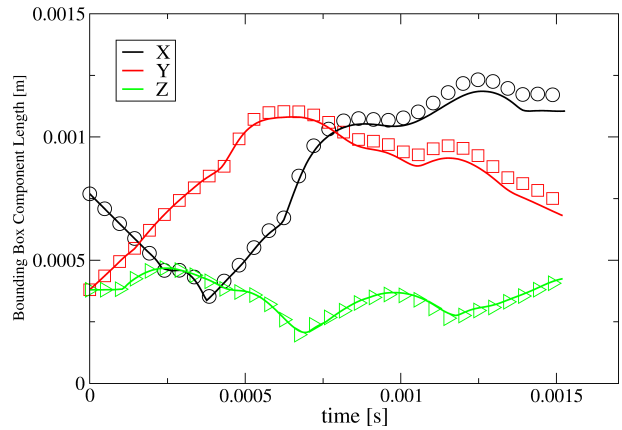


Figure 8: A comparison of the domain bounding box dimension lengths between test meshes. Symbols: approx. 440k tetrahedra, Solid Lines: approx. 110k tetrahedra. The maximum mesh-to-mesh droplet shape discrepancy throughout the simulation is 5.47%.

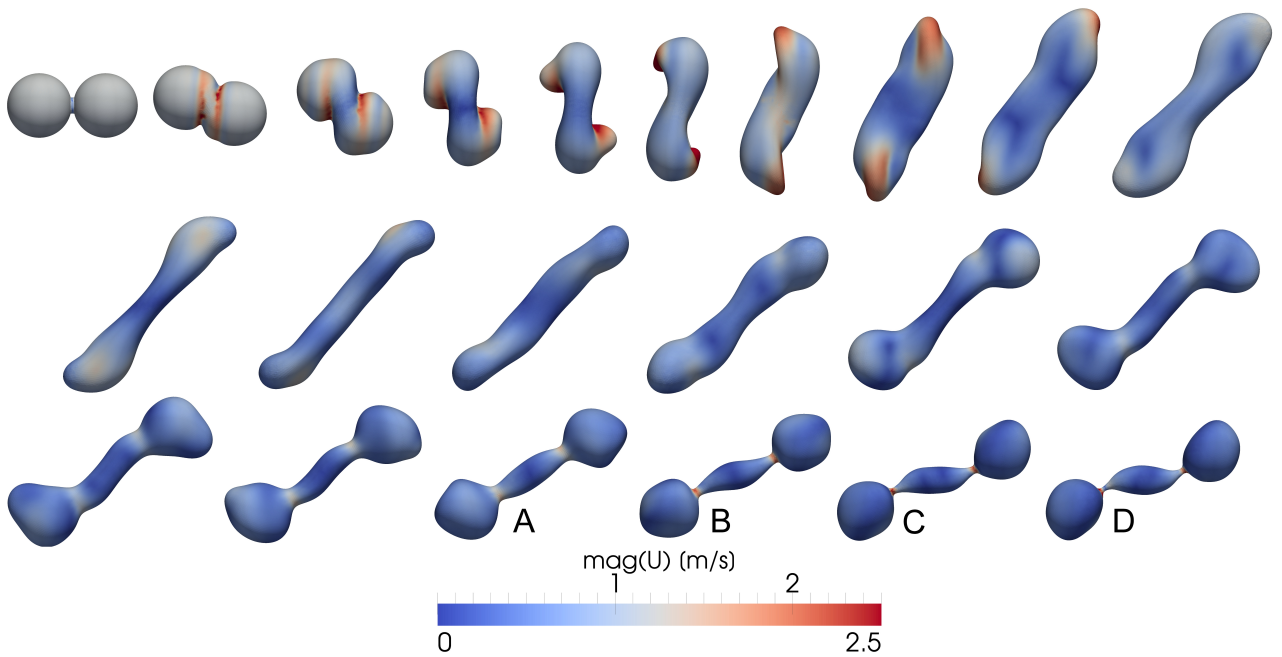


Figure 9: Profile snapshots of a viscoelastic droplet collision. $\chi = 0.68$, $We = 28.7$, $Re = 874$, $De = 0.2$. The time duration between images is $8e-5$ [s]. The surface is colored by velocity magnitude. Stress profiles of frames A through D are illustrated in Fig.10.

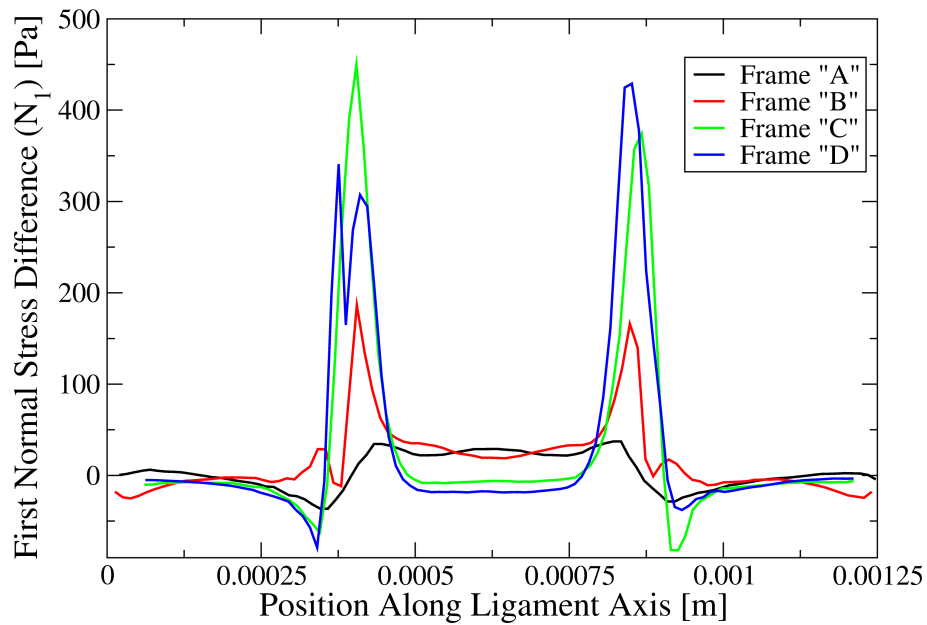


Figure 10: Line samples of the first normal stress difference ($N_1 = \tau_{xx} - \tau_{yy}$) of the frames labeled A through D in Fig.9. The sample line was re-oriented each time step to be co-axial with the ligament. Stress peaks correspond spatially to the two pinch off points between the middle ligament and two satellite droplets.

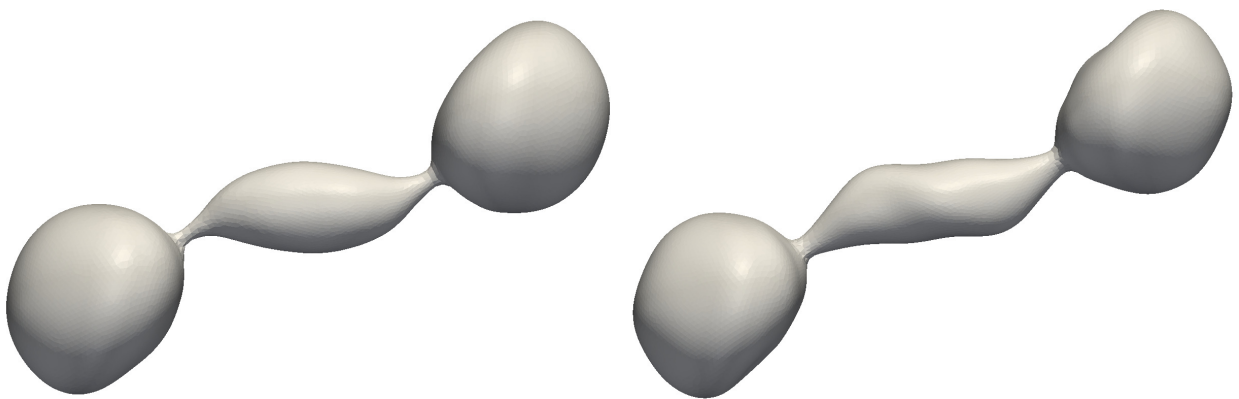


Figure 11: Time paired side-by-side comparison of the final stages of two droplet collisions. Collision parameters: $\chi = 0.68$, $We = 28.7$, $Re = 874$, Left: $De = 0.2$, Right: $De = 2.0$. Time = 0.001632 [s].

Summary and Conclusions

In this work, finite volume CFD simulations on a dynamic tetrahedral mesh were performed in an effort to simulate the collision of viscoelastic droplets. The interface modeling method (moving mesh interface tracking) was validated with analytical expressions while the implementation of the linear Phan-Thien Tanner viscoelastic stress equations was validated against experimental observations of velocity and stress profiles in a channel flow.

The effects of mild viscoelasticity were observed in simulation results to occur in the late stages of the droplet collision process, e.g. ligament collapse and pinch off. Thus far the collisions simulated at $We = 28.7$ and $0.2 \leq De \leq 2.0$ numbers showed little effects of viscoelasticity previous to the pinch off stage. Inhibiting pinchoff in this manner could reduce the formation of smaller satellite droplets and tighten the droplet size distribution in an atomizing viscoelastic spray.

Future work will include comprehensive parametric studies to span a larger range of dimensionless groups such as χ , We , and De in an attempt to quantify the effects of viscoelasticity on droplet collisions. Higher De collisions should, in theory, show elastic effects earlier than the punch off stage in the collision process. In order to model fluids of higher viscoelasticity, however, methods such as the log-conformation tensor approach by Fattal and Kupferman [23] may be required to overcome the high Weissenberg number stability limit.

Acknowledgments

The authors would like to acknowledge the financial support of the Army Research Office under grant number W911NF-08-1-0171. Computations in this work utilized the Extreme Science and Engineering Discovery Environment (XSEDE), which is supported by National Science Foundation grant number OCI-1053575. We also thank Hrvoje Jasak, Zeljko Tuković, and Jovani Favero for OpenFOAM software library contributions.

References

- [1] Schmidt, D.P., Rutland, C.J. *Journal of Computational Physics* (2000)
- [2] Gavaises, M. *Journal of Mechanical Engineering Science* 210:456-477 (1996)
- [3] Qian, J., Law, C. K. *Journal of Fluid Mechanics* (1997)
- [4] Ashgriz, N., Poo, J.Y. *Journal of Fluid Mechanics* 221:183-204 (1990)
- [5] Willis, K., Orme, M. *Experiments in Fluids* 34:28-41 (2003)
- [6] Menon, S., Rothstein, J. Schmidt, D.P. *11th Triennial International Conference on Liquid Atomization and Spray Systems, Vail, Colorado, USA* (2009)
- [7] Rahimi, S., Peretz A. *Propellants, Explosives, Pyrotechnics* 32:165-174 (2007)
- [8] Motzigemba, M., Roth, N., Bothe, D., Warnecke, H. J. *ILASS-Europe* (Sept. 2002)
- [9] Focke, C., Bothe, D. *ILASS-Europe* (Sept. 2010)
- [10] Rahimi, S., Weihs, D. *Propellants, Explosives, Pyrotechnics* 36:273-281 (2011)
- [11] Yue, P., Feng, J., Liu, C., Shen, J. *Journal of Non-Newtonian Fluid Mechanics* 129:163-176 (2005)
- [12] Weller, H. G., Tabor, G., Jasak, H., Fureby, C. *Computers In Physics* 12:620-631 (1998)
- [13] Tukovic, J., Jasak, H. *Computers & Fluids* (2012)
- [14] Dai, M., Schmidt, D. P. *Journal of Computational Physics* 208:228-252 (2005)
- [15] Menon, S., Schmidt, D. P. *Comput. Methods Appl. Mech. Engrg.* 200:2797-2804 (2011)
- [16] Aplsey, D., Hu, W. *Intl. Journal for Numerical Methods in Fluids* 42:465-491 (2003)
- [17] Lamb, H. *Proc. London Mathematic Society* (1881)
- [18] Favero, J.L., Secchi, A.R., Cardozo, N.S.M., Jasak, H. *Journal of Non-Newtonian Fluid Mechanics* 165:1625-1636 (2010)
- [19] Phan-Thien, N., Tanner, R.I. *Journal of Non-Newtonian Fluid Mechanics* 2:353-365 (1977)
- [20] Azaiez, J., Guenette, R., AitKadi, A. *Journal of Non-Newtonian Fluid Mechanics* (1996)
- [21] Quinzani, L., Armstrong, R.C., Brown, R.A. *Journal of Non-Newtonian Fluid Mechanics* (1994)
- [22] Xue, S. C., Tanner, R. I., Phan-Thein, N. *Journal of Non-Newtonian Fluid Mechanics* (2004)
- [23] Fattal, R, Kupferman, R. *Journal of Non-Newtonian Fluid Mechanics* (2004)